CHEMISTRY OF MATERIALS

pubs.acs.org/cm Article

A Synergistic Approach to Unraveling the Thermodynamic Stability of Binary and Ternary Chevrel Phase Sulfides

Kristina Lilova,[⊥] Joseph T. Perryman,[⊥] Nicholas R. Singstock,[⊥] Mykola Abramchuk, Tamilarasan Subramani, Andy Lam, Ray Yoo, Jessica C. Ortiz-Rodríguez, Charles B. Musgrave,* Alexandra Navrotsky,* and Jesús M. Velázquez*

Cite This: *Chem. Mater.* 2020, 32, 7044−7051 Read Online

ABSTRACT: State-of-the-art high temperature oxide melt solution calorimetry and density functional theory were employed to produce the first systematic study of thermodynamic stability in a series of binary and ternary Chevrel phases. Rapid microwave-assisted solid-state heating methods facilitated the nucleation of pure-phase polycrystalline $M_yMo_6S_8$ (M = Fe, Ni, Cu; y = 0, 1, 2) Chevrel phases, and a stability trend was observed wherein intercalation of M_y species engenders stability that depends on both the electropositivity and ionic radii of the intercalant species. *Ab initio* calculations indicate that this stability trend results from competing ionic and covalent contributions, where transition metal intercalation stabilizes the Chevrel structure through increased ionicity but destabilizes the structure through reduced covalency of the Mo_6S_8 clusters. Our calculations predicted that over intercalation of high-valent M_y species leads to slight destabilization of the Mo_6 octahedral cores, which we confirm using calorimetry and X-ray absorption spectroscopy. Our combined computational and calorimetric analysis reveals the interplay of the foundational principles of ionic and covalent bonding characteristics that govern the thermodynamic stability of Chevrel and other inorganic phases.

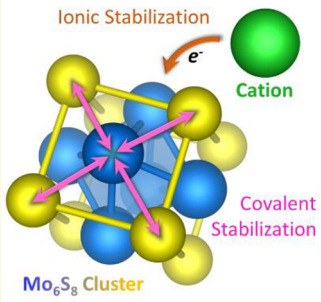

■ INTRODUCTION

The immense body of work demonstrating binary and ternary chalcogenides for a wide variety of applications, along with their conspicuous compositional and structural tunability, make them especially attractive solid-state inorganic frameworks to develop formalisms for material properties that transcend specific crystal structures and compositions.[1−12] Chevrel phases (CPs) constitute a fascinating subset of the chalcogenide family with highly flexible compositions of the general formula $M_yMo_6X_8$ (M = alkali, alkaline earth, transition, or post-transition metal, y = 0−4, X = S, Se, Te) and equally flexible—albeit composition-dependent—synthetic accessibility. Successful synthesis of these materials has been reported via traditional solid-state methods,[5,13,14] rapid microwave-assisted methods,[7,15] self-propagating combustion methods,[16] and thin-film conversion methods,[17] among others. Although these materials have been extensively characterized as multivalent ion intercalation cathodes during reversible battery cycling,[1−3,10,11,18−23] alternative applications for this chalcogenide family are abundant. Previous characterization suggests that these materials have promising applications as thermoelectrics,[24,25] as superconductors,[4−6] and as energy-conversion catalysts,[7,8,26,27] where tunable electronic characteristics can be leveraged to induce favorable charge carrier propagation and adsorption kinetics.[28] It has been observed that intercalation by metallic species leads to donation of electron density into Mo_6X_8 clusters (Figure 1A), thereby both altering the electronic structure of the chalcogen site[29,30] and—by modulation of intracluster Mo−Mo bond distances[31]—affording control over the d-band structure that is of critical importance for tuning electron-transfer kinetics.[32−34] The strongly composition- and structure-dependent properties of CP materials and of chalcogenides in general make them a rich space for discovering novel materials and motivated our application of a combination of experimental and computational approaches to understand and predict the thermodynamic stability of these compositionally flexible solid-state frameworks.

The CP structure is composed of Mo_6 octahedra that exist inside a stabilizing pseudocubic X_8 cage to form Mo_6X_8 molecular building blocks, from which three-dimensional networks are extended via intercluster Mo−X bonds. As shown in Figure 1A, the space between adjacent Mo_6X_8 clusters (blue and yellow) forms prismatic cavities that can accommodate cation intercalation (green), thereby allowing for compositional modification and subsequent stabilization/destabilization of the network of interconnected binary

Received: June 23, 2020
Revised: July 28, 2020
Published: July 29, 2020

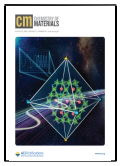

https://dx.doi.org/10.1021/acs.chemmater.0c02648
Chem. Mater. 2020, 32, 7044−7051

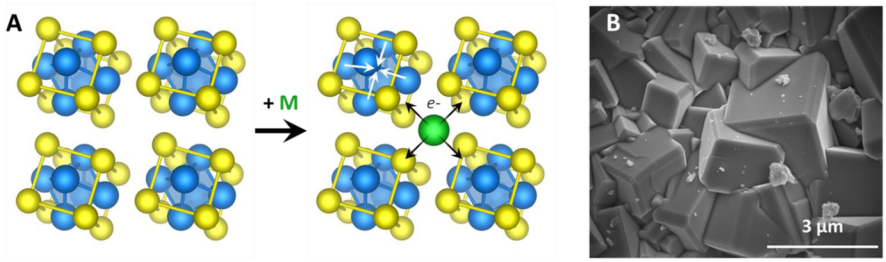

Figure 1. (A) Crystal structure representation of the Mo_6S_8 phase where Mo_6 octahedra (blue) are surrounded by S_8 (yellow) pseudocubes, forming an extended network of cavities into which ternary metal species (green) can intercalate and donate electron density to the electron-deficient Mo_6S_8 units, leading to contraction of the Mo octahedra. (B) Representative SEM micrograph illustrating the faceted morphology of as-synthesized polycrystalline CPs studied here. The intercluster Mo−S linkages have been omitted for clarity.

clusters. Multinary CPs are classified as two general types based on the intercalated cation(s): type I phases with large cations such as Pb, Sn, Ag, and La and type II phases with small cations such as Li, Na, Cu, Ni, Co, and Fe.[35,36] This provides two promising avenues to pursue in investigating the effect of ternary element composition and properties on local coordination and electronic structure in these highly versatile chalcogenide phases.

Cation intercalation is a common route for stabilizing the binary Mo_6X_8 structures, which are intrinsically electron deficient.[37] For instance, Mo_6S_8 is synthesized indirectly by first making the cation-stabilized ternary phase $Cu_2Mo_6S_8$ and then leaching the cation.[38,39] However, the intercalated cations cause competing stabilizing and destabilizing effects that depend sensitively on the identity of cation M and its stoichiometry, *y*. Electron donation from the intercalant to the Mo_6S_8 cluster stabilizes the electron-deficient structure and leads to contraction of the Mo octahedra (Figure 1A).[40] Conversely, larger cations (type I CPs) result in higher strain and destabilization of the structure due to steric mismatch between the cations and the Mo_6S_8 clusters, while over intercalation of smaller cations (type II CPs) destabilizes the structure via increased population of Mo antibonding states.[37] Although previous reports describe how cation intercalation affects CP structure and stability, they do not provide a fundamental description of how these stabilizing and destabilizing effects arise.

Additional efforts have been dedicated to developing a working understanding of the structural and electronic drivers of stability domains for superconducting and thermoelectric CPs based on assumptions about their conduction band population after metal intercalation or chalcogen substitution.[9] However, quantitative calorimetric studies of CP sulfides remain scarce.[41] In addition, such studies are often focused exclusively on Mg intercalation stability,[2] although the breadth of applications for this material family suggests that reliable descriptors of phase stability in a wider range of compositions are highly desirable. It has been observed that cation intercalation into the CP structure has a pronounced effect on their relative stability as rhombohedral versus triclinic phases,[42] especially for phases with varied 3d M_y compositions. Hence, the purpose of the current study is to investigate the effect of small-cation (type II) incorporation on the thermodynamic properties of four ternary CPs: $FeMo_6S_8$, $Fe_2Mo_6S_8$, $Ni_2Mo_6S_8$, and $Cu_2Mo_6S_8$. This work provides a fundamental description of the effects of cation intercalation on thermodynamic stability through a synergistic experimental and computational study. This work also highlights the rewards of rationally integrating insights gleaned from computational analysis with observed trends in structure and stability, toward an iterative feedback between experiment and theory that can drive novel material design.

■ EXPERIMENTAL METHODS

Synthesis. MoS_2 powder (>99.5%, 325 mesh), Fe powder (99.998%, 22 mesh), Cu powder (99.995%, 100 mesh), and Ni powder (99.8%, 325 mesh) were used as purchased from Alfa Aesar. Mo powder (99.99%, 100 mesh) was used as purchased from Sigma-Aldrich.

CPs were synthesized according to methods described in work by Perryman et al.[7,31] Briefly, high temperature solid-state reactions were carried out in silica tubes under N_2 using pellets comprised of stoichiometric amounts of high-purity (>99.5%) elemental powders of Cu, Fe, Ni, and Mo, as well as MoS_2 powder as a sulfur source, according to the reaction

$$yM + 2Mo + 4MoS_2 \rightarrow M_yMo_6S_8 \quad (1)$$

Microwave irradiation[43]—coupled with a graphitic microwave susceptor[44,45]—facilitated rapid conversion of incident radiation into thermal energy where temperatures were maintained at ∼1273 K for 10 min for each metal-intercalated CP. In order to obtain binary Mo_6S_8, wet chemical etching was employed according to methods discussed by Lancry et al. where $Cu_2Mo_6S_8$ was stirred overnight in a 6 M HCl solution with O_2 bubbling.[38]

Characterization. Phase purity of synthesized CPs was characterized via powder X-ray diffraction (PXRD) on a Bruker D8 Advance diffractometer with Cu Kα radiation (1.5406 Å), after which experimental PXRD patterns were compared with predicted patterns to confirm formation of the correct phase. The morphology of CPs (depicted in Figure 1B) was characterized using an FEI (Hillsboro, OR) Nova NanoSEM 430. Composition was confirmed via energy-dispersive X-ray spectroscopy (EDS) (Figure S1) on an FEI Scios dual beam SEM/FIB with an Oxford EDS detector. CP electronic structure and local Mo coordination were observed via X-ray absorption spectroscopy (XAS) at the Stanford Synchrotron Radiation Lightsource (SSRL). The Mo K-edge was probed at beamline 4-1, while Fe, Ni, and Cu K-edges as well as S K-edge and Mo L-edges were probed at beamline 4-3. Elemental foils were used as references for energy calibration in all cases except for S K-edge and Mo L-edges, where $Na_2S_2O_3$ was used as a reference. Scans were performed in triplicate and averaged to increase the signal-to-noise ratio.

High Temperature Oxide Melt Solution Calorimetry. High temperature drop solution calorimetry was performed using a Tian Calvet twin calorimeter AlexSYS (Setaram, France) at 1073 K as described previously.[46−48] The small temperature difference between the sample and its constant surroundings, namely a large metal block heat sink, registered by a thermopile, is proportional to the heat flow. The integral of the thermopile emf in a calorimetric peak generated by a chemical reaction, relative to an established baseline, is proportional to the heat effect and, with appropriate calibration, gives the enthalpy

https://dx.doi.org/10.1021/acs.chemmater.0c02648
Chem. Mater. 2020, 32, 7044−7051

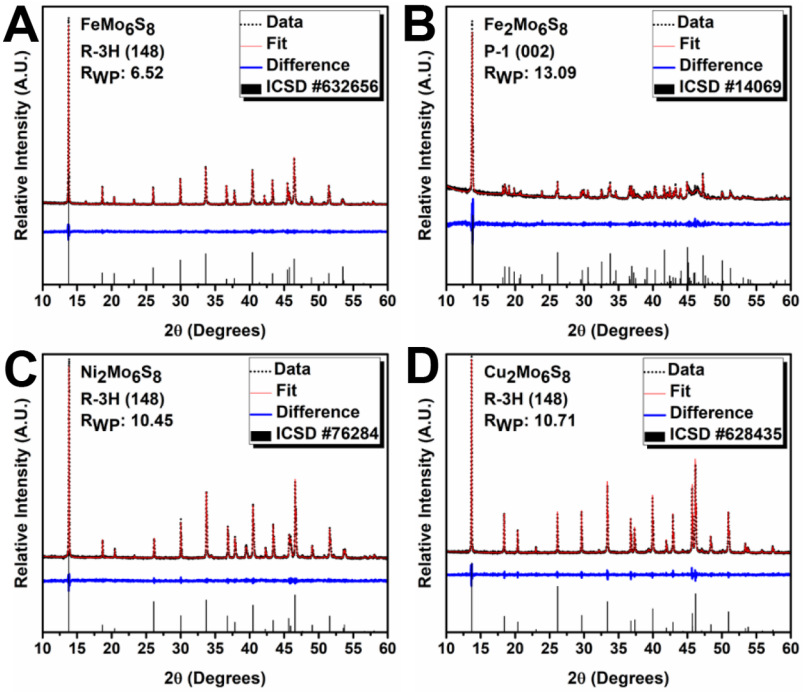

Figure 2. PXRD refinement results for synthesized (A) $FeMo_6S_8$, (B) $Fe_2Mo_6S_8$, (C) $Ni_2Mo_6S_8$, and (D) $Cu_2Mo_6S_8$. Gray ticks represent positions and relative intensities of reflections expected from published ICSD patterns.

of reaction. In the experiments reported here, the powdered samples were pressed into pellets and dropped into a platinum crucible containing molten sodium molybdate $3Na_2O{\cdot}4MoO_3$ solvent. Pure oxygen gas was flushed over the solvent at 90 mL/min and bubbled through it at 5 mL/min. The bubbling gas brings the samples into much more direct contact with an oxidizing environment, speeds oxidation, and stirs the solvent. The calorimeter was calibrated against the heat of combustion of 5 mg pellets of benzoic acid ($C_7H_6O_2$, Parr Instruments).

The measured drop solution enthalpy represents the sum of heat content of the sample from room temperature to 1073 K, its heat of solution in the sodium molybdate melt, and its heat of oxidation. Because the heat of oxidation is the largest contribution to the drop solution enthalpy, all values are expected to be negative. More details on the procedure are given by Hayun et al. and Abramchuk et al.[49,50] The drop solution enthalpy is then used to calculate the enthalpies of formation from components or from elements. For such a calculation to be valid, one must be certain the initial state of the oxides immediately prior to dissolution is known and the final state of the oxides in the melt is well-defined and reproducible.

Computations. Density functional theory (DFT) calculations were performed using the Vienna Ab initio Simulation Package (VASP).[51] The Strongly Constrained and Appropriately Normed (SCAN)[52] semilocal density functional was used to compute ground-state structures, total energies, and density of states (DOS) for the compounds and elements. All calculations were performed with a plane wave cutoff of 520 eV and a Γ-centered Monkhorst−Pack *k*-point grid with a density of 1200/*N*, where *N* is the number of atoms in the unit cell. Charge densities were calculated using DDEC6 atomic population analysis which partitions net atomic charges within solid-state structures.[53] Oxidation states were determined for each species by taking the difference between their calculated charge densities and standard valence electron counts, followed by normalization so that the oxidation state of sulfur was −2 in each structure. Madelung energies were computed from DDEC6 charges using the Ewald summation method implemented in Pymatgen and then normalized by the number of sulfur atoms to determine the degree of ionicity in the studied structures.[54] Crystal orbital overlap populations (COOPs) were calculated using LOBSTER.[55] Sigma (Σ) values are the energy weighted integral of the Mo−S bonding and antibonding states of the COOP from −14 eV to the Fermi level and are used to determine the degree of covalency in the studied structures because they all contain Mo−S bonds; sigma values were calculated using a python script available at https://github.com/CJBartel/compmatscipy.[56]

■ RESULTS AND DISCUSSION

PXRD patterns (Figure 2) indicate that each CP of interest was synthesized with high phase purity, with $FeMo_6S_8$, $Ni_2Mo_6S_8$, and $Cu_2Mo_6S_8$ exhibiting a rhombohedral $R\bar{3}H$ crystal structure and $Fe_2Mo_6S_8$ exhibiting a slightly distorted triclinic $P\bar{1}$ crystal structure—all of which exhibit lattice parameters in good agreement with the literature (Table S1).[57]

Drop solution enthalpies and experimental enthalpies of formation from components and elements of all compounds are reported in Table S2 and Figure 3. All values have been calculated per gram atom.

Experimental enthalpies of formation from components and elements were calculated at 298 K from the thermodynamic cycles shown in Tables S3 and S4, respectively. The drop solution enthalpy of pure molybdenum metal was verified using the new oxidative high temperature solution calorimetry methodology, described by Hayun et al.[49] We note that, because all ternary CPs have similar structures, their entropies can be assumed to be similar in magnitude; i.e., trends in thermodynamic stability are dictated by the enthalpies of formation.

Calorimetric measurements indicate that iron incorporation in the Mo_6S_8 structure promotes the thermodynamic stability of the ternary sulfides; i.e., the enthalpies of formation from pure elements, from sulfide components, and from Mo_6S_8 intercalation follow the trend $FeMo_6S_8$ < $Fe_2Mo_6S_8$ < $Ni_2Mo_6S_8$ < $Cu_2Mo_6S_8$. The enthalpies of formation from elements are negative for all compounds (Table S2). The enthalpies of formation from the metal and the binary Mo_6S_8 according to the reaction

https://dx.doi.org/10.1021/acs.chemmater.0c02648
Chem. Mater. 2020, 32, 7044−7051

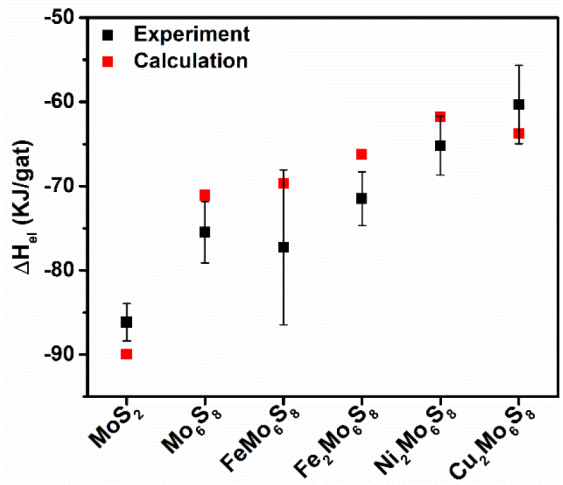

Figure 3. Experimental and computation enthalpies of formation from elements for $M_yMo_6S_8$ and MoS_2, illustrating good agreement in the stability trend within the propagated error of the experimental enthalpy measurements. Error bars represent propagated error according to the calculation steps outlined in Table S4. Errors for calorimetric data are presented as two standard deviations of the mean, which was less than 2% for all elements and compounds.

$$yM + Mo_6S_8 \rightarrow M_yMo_6X_8 \quad (2)$$

are negative for both $Fe_2Mo_6S_8$ and $FeMo_6S_8$, while the values for $Ni_2Mo_6S_8$ and $Cu_2Mo_6S_8$ are slightly positive or approximately zero within the experimental error. The trend in the thermodynamic stability of the four CPs with respect to the cation incorporation in the Mo_6S_8 matrix can also be seen from the enthalpies of the synthesis reaction

$$yM + 2Mo + 4MoS_2 \rightarrow M_yMo_6X_8 \quad (3)$$

Because of the relatively large experimental error, the enthalpy of formation from the synthesis reaction 3 of $Cu_2Mo_6S_8$ can be considered close to zero, but probably still slightly positive.

The difference in the thermodynamic stabilities of the small cation CPs can be attributed to the increased valency (i.e., increased charge donation) of the intercalated cations (Fe > Cu > Ni). Greater electron donation (up to four electrons to Mo_6S_8) from cations with increased valency results in more pronounced contraction of the Mo_6 octahedron because the HOMO and LUMO of isolated Mo_6S_8 clusters are predominately Mo−Mo bonding in nature. Previous EXAFS fitting,[31] XRD, and DFT geometries indicate that the average Mo−Mo bond distance decreases ($Fe_2Mo_6S_8$ < $Cu_2Mo_6S_8$ < $Ni_2Mo_6S_8$) as cation valency increases (Fe > Cu > Ni). Furthermore, XAS analysis suggests that Fe is more oxidized in $FeMo_6S_8$ compared to $Fe_2Mo_6S_8$ (Figure 4), in good agreement with the calculated cation charge in each structure. While we do not present a quantitative analysis of cation charge density based upon the onset energy for 1s → 4p excitations represented in the rising edge positions shown in Figure 4, XAS is in good agreement with the results of our DDEC6 atomic population analysis. This suggests that experimental elucidation of cation charge density via XANES analysis in accordance with Kunzl's rule[58] is a viable method for estimating the degree of ionicity in these frameworks. All the results indicate an increase in electron donation from the intercalated cation to the Mo_6S_8 cluster as valency increases, which stabilizes the structure.

ΔH_f values at 0 K computed using DFT (Table S5) match experimental results well, as illustrated in Figure 3. The calculated and the experimental ΔH_f values for the binary Mo_6S_8 are also consistent with the values of Hinode et al.[41] Differences in the stability ordering between computation (0 K) and experiment (298 K) can be attributed to temperature differences and the resolution of our methods. DFT results indicate that the formation enthalpies of the studied ternary CPs decrease as the electropositivity and the stoichiometry of the intercalated cation increases ($Fe_2Mo_6S_8$ < $FeMo_6S_8$ < $Cu_2Mo_6S_8$ < $Ni_2Mo_6S_8$). This increase in electropositivity, and a corresponding increase in valency, leads to an increase in the Mo_6 cluster charge density indicated by a decreasing average Mo oxidation state (1.77, 1.90, 2.00 for M_y = Fe_2, Cu_2, Ni_2, respectively), as shown in Table S6. The average Mo oxidation state for $FeMo_6S_8$ (2.00) is greater than that for $Fe_2Mo_6S_8$ (1.77), matching the computational trend in stability. However, the oxidation state of Fe in $FeMo_6S_8$ (3.98) is greater than in $Fe_2Mo_6S_8$ (2.70 average) which indicates that the first Fe intercalated into the Mo_6S_8 framework transfers more electron density to the Mo_6 cluster and therefore yields a greater decrease in ΔH_f relative to the second Fe. This matches with the 1 eV blue-shifted Fe K-edge XANES for $FeMo_6S_8$ versus $Fe_2Mo_6S_8$ in Figure 4A. Thus, both the electropositivity and the stoichiometry of the intercalated cation affect the electron donation to the Mo_6S_8 cluster and the resultant stabilizing contribution to the ternary CP.

The mechanism for ternary CP stabilization results from competing ionic and covalent contributions. The Madelung

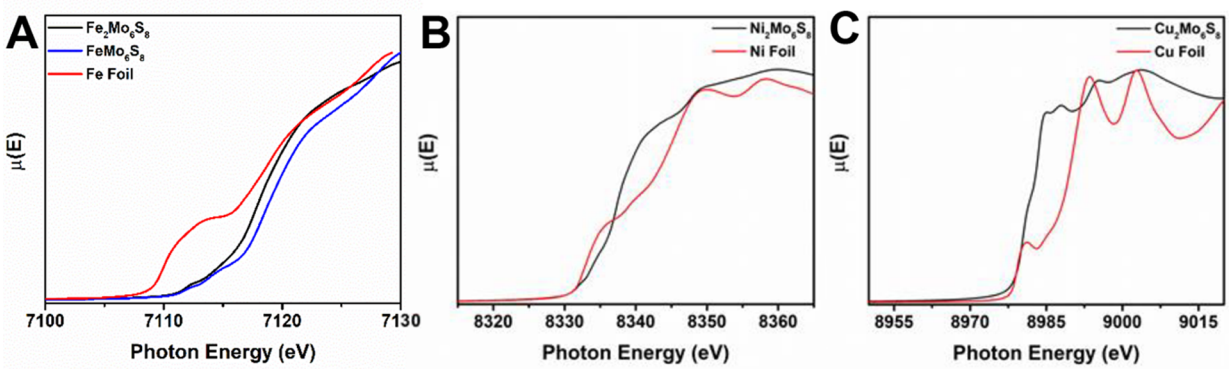

Figure 4. (A) Fe K-edge XANES for $FeMo_6S_8$ (blue), $Fe_2Mo_6S_8$ (black), and a Fe reference foil (red). (B) Ni K-edge XANES for $Ni_2Mo_6S_8$ (black) and a Ni reference foil (red). (C) Cu K-edge XANES for $Cu_2Mo_6S_8$ (black) and a Cu reference foil (red).

https://dx.doi.org/10.1021/acs.chemmater.0c02648
Chem. Mater. 2020, 32, 7044−7051

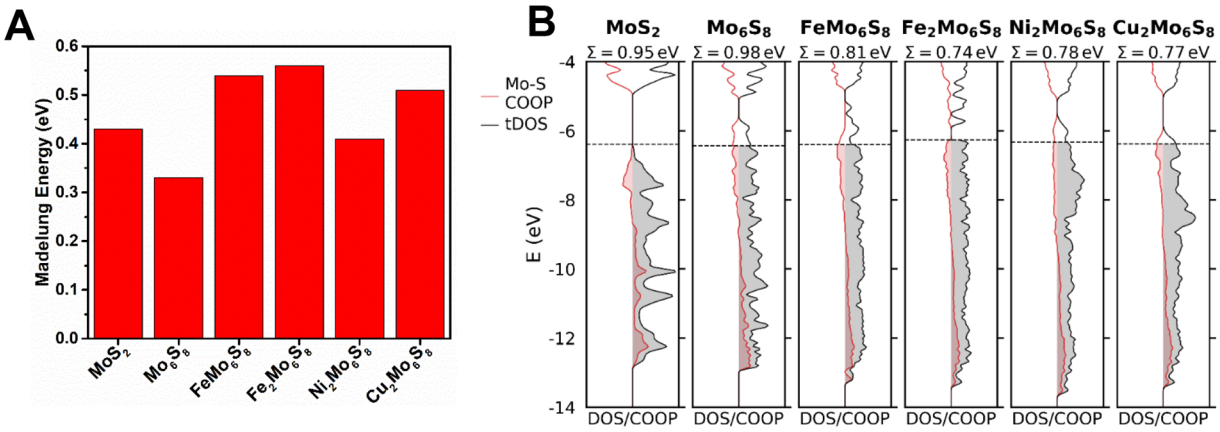

Figure 5. (A) Madelung energies of the five CPs and MoS_2, normalized by the number of sulfur atoms in the structure to enable comparison between CPs and MoS_2. A greater Madelung energy indicates stronger ionicity. (B) Total density of states (DOS, black line) and crystal orbital overlap population (COOP, red line) of Mo and S atoms for the five CPs and MoS_2. Positive COOP values indicate covalent bonding states, and negative values indicate covalent antibonding states. Σ is the energy integrated COOP from −14 eV to the Fermi level (dashed line) which indicates the net covalent bonding between Mo and S in these structures.

energy of a material is a measure of the interatomic electrostatic interactions (i.e., the ionicity).[59,60] Figure 5A shows the Madelung energies of the studied materials, indicating a greater overall ionicity as the electropositivity and stoichiometry of the intercalated cations increase (Fe_2 > Fe > Cu_2 > Ni_2) due to a greater dipole moment between the chalcogenide and the cation. For the ternary CPs, a greater ionicity results in a lower computational ΔH_f. Similarly, the inherent stability of MoS_2 over Mo_6S_8 can be explained by the greater ionicity of MoS_2. However, the Madelung energy alone would suggest greater ionicity, and thus stability, of $Ni_2Mo_6S_8$ over Mo_6S_8 and is therefore an incomplete descriptor for stability. A similar study on nitrides showed that covalent bonding should also be considered to provide a more complete description of material stability.[56]

Figure 5B shows the total electronic density of states (DOS) and the COOP between Mo and S for the studied materials. Positive and negative COOP values indicate covalent bonding and antibonding states, respectively. The net covalent bonding (i.e., covalency) between Mo and S is indicated by Σ. For the CPs, Mo_6S_8 exhibits the greatest Σ, consistent with the shorter Mo−S bond distance in this material. Intercalating cations into the Mo_6S_8 framework increases the charge density on Mo via electron donation from the cation, thereby decreasing the Mo−S bond strength and elongating the Mo−S bond, which leads to a decrease in covalency and destabilization of the CP structure. Thus, as the total oxidation state of the intercalant cations increases (Table S6) due to an increase in valency, the degree of covalency (Σ) decreases. This decrease in Σ trends with an increase in the ionic radii (0.92, 0.87, and 0.83 Å for Fe^{2+}, Cu^{2+}, and Ni^{2+}, respectively)[61] and stoichiometry of the intercalant cation for the studied transition metals. For all the ternary CPs except $Ni_2Mo_6S_8$, the stabilization from an increase in ionicity is greater than the destabilization due to the loss of covalency at 0 K. Although all the materials have filled antibonding states, $Fe_2Mo_6S_8$ and $Cu_2Mo_6S_8$ have the lowest Σ values due to a greater filling of Mo−S antibonding states, which corresponds to electron donation from the intercalants to the Mo_6S_8 cluster that exceeds four electrons. The large Σ value of MoS_2 combined with its moderate Madelung energy explains the low computational ΔH_f of MoS_2 and the positive decomposition enthalpy to MoS_2 ($\Delta H_{f(3)}$) for the ternary CPs at 0 K. Unlike the bonding analysis results from ref 32, no large variation in sulfur charge is predicted for any of the studied materials, and the innate instability of Mo_6S_8 is instead attributed to its relatively low ionicity. This increase in ionicity and reduction of covalency upon intercalation of a metallic species is represented in Figure 6.

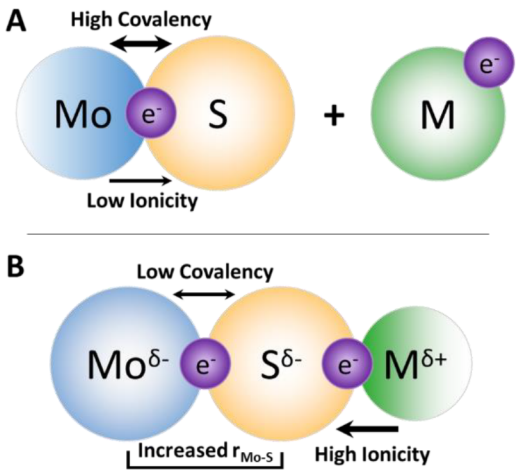

Figure 6. Reductive effects of M species intercalation into Mo_6S_8, which decrease the covalency of the Mo−S interactions observed in binary Mo_6S_8 and increase the relative charge on Mo and S to yield a net increase in ionic bonding character within the structure.

Calorimetric data suggests that, at 298 K, $Fe_2Mo_6S_8$ is metastable with respect to $FeMo_6S_8$. This also agrees well with Mo−Mo bond distances observed in X-ray diffraction analysis where average Mo−Mo distances in $FeMo_6S_8$ are approximately 2.679 Å as compared to 2.682 Å in $Fe_2Mo_6S_8$. This destabilization of $Fe_2Mo_6S_8$ may be the result of a slight degree of triclinic distortion in the $Fe_2Mo_6S_8$ structure where Mo_6S_8 cluster units are tilted with respect to the original rhombohedral axis,[40] thereby allowing more structural flexibility and slight deformation of the Mo_6 octahedral symmetry which is observed at 298 K but not at 0 K. This also matches with our computational results that indicate greater filling of antibonding Mo−S states in $Fe_2Mo_6S_8$, which

https://dx.doi.org/10.1021/acs.chemmater.0c02648
Chem. Mater. 2020, 32, 7044−7051

decreases covalency and destabilizes the structure. A similar destabilization is observed for MoS_2 where DFT predicts that this material is more stable than Mo_6S_8 and the ternary CPs at 0 K, in good agreement with published literature.[14,38,62] However, calorimetry indicates that Mo_6S_8 is slightly more stable than MoS_2 at 298 K, although this is within the experimental error. The small formation enthalpy difference between these materials explains why Mo_6S_8 cannot be directly synthesized at 298 K but is persistently metastable at this temperature. Additionally, the propensity of Mo_6S_8 to decompose to Mo and MoS_2 at high temperatures is consistent with the observation that an intercalant such as Cu is required to stabilize the Mo_6S_8 structure at high temperature, despite $Cu_2Mo_6S_8$ having a slightly more positive formation enthalpy than Mo_6S_8 at 298 K.

Furthermore, this work may help elucidate a fundamental description of cation diffusivity and stability relevant to CP electrodes for monovalent (e.g., Li, Na) and multivalent (e.g., Mg) ion batteries. Highly electropositive cations (e.g., Li^+, Na^+, Mg^{2+}) should yield CP structures with high ionicity, due to large dipole moments with the chalcogenide, and similar covalency to the studied transition metal intercalants due to similar electron donation. These CP electrodes would therefore be expected to demonstrate greater stability and lower diffusivity than the studied ternary CPs, matching experimental observations that less electropositive 3d metals such as Mn^{2+}, Fe^{2+}, Co^{2+}, and Zn^{2+} exhibit high diffusivities on the order of 10^{-9} cm^2/s,[63] whereas the more electropositive Mg^{2+} exhibits a much lower diffusivity on the order of 10^{-12} cm^2/s.[1] Similarly, for Mg intercalation, substituting Se for S yields a higher diffusivity, which may result from the lower dipole moment, and thus ionicity, between Mg and the chalcogenide,[64] although further analysis is required to confirm this hypothesis.

■ CONCLUSION

We have successfully implemented rapid microwave-assisted synthesis for a series of 3d transition metal-intercalated CP sulfides and have employed highly reliable calorimetric and computational methods to elucidate trends in thermodynamic stability as a function of intercalant stoichiometry and electropositivity. Stability in the studied CP sulfides results from a competition between ionic and covalent contributions, where intercalation of 3d transition metals into Mo_6S_8 increases the overall ionicity of the structure while decreasing the covalent bonding between Mo and S. A greater increase in ionicity is predicted as the electropositivity and stoichiometry of the intercalant increase due to increased charge donation from the intercalant to the Mo_6S_8 cluster and a greater dipole strength between the cation and chalcogenide. Conversely, covalent bonding between Mo and S in the Mo_6S_8 cluster decreases as the ionic radius and stoichiometry of the cation increase due to an increase in valency. These competing effects determine the formation enthalpy, and thus stability, of the CPs at 0 K, where increased ionicity and covalency yield a lower formation enthalpy. As the temperature increases, additional destabilization can occur through distortion of the structure, as is observed for $Fe_2Mo_6S_8$.

This work represents the first experimental and computational study of the thermodynamics of a binary or ternary CP chalcogenide. Proof of the efficacy of our integrated calorimetric−spectroscopic−computational approach to material evaluation will drive future efforts to expand the existing library of thermodynamic information for the rich composition space of transition metal chalcogenides. This integrated approach will significantly accelerate materials discovery with the goal of developing state-of-the-art materials that operate under extreme conditions such as those that are required for deep space exploration. This avenue of materials discovery will also catalyze an effort to rationally design new stable energy conversion and storage materials based on the Chevrel framework where reactivity and energy capacity optimization require fine compositional control as well as reliable models for predicting structural stability.

■ ASSOCIATED CONTENT

Supporting Information

The Supporting Information is available free of charge at https://pubs.acs.org/doi/10.1021/acs.chemmater.0c02648.

Compositional analysis and tables with all data and thermochemical cycles that are discussed in this work (PDF)

■ AUTHOR INFORMATION

Corresponding Authors

Jesús M. Velázquez − *Department of Chemistry, University of California Davis, Davis, California 95616, United States;* orcid.org/0000-0003-2790-0976; Email: jevelazquez@ucdavis.edu

Alexandra Navrotsky − *School of Molecular Sciences and Center for Materials of the Universe, Arizona State University, Tempe, Arizona 85287, United States;* orcid.org/0000-0002-3260-0364; Email: alexandra.navrotsky@asu.edu

Charles B. Musgrave − *Department of Chemical and Biological Engineering, University of Colorado Boulder, Boulder, Colorado 80309, United States;* orcid.org/0000-0002-5732-3180; Email: charles.musgrave@colorado.edu

Authors

Kristina Lilova − *School of Molecular Sciences and Center for Materials of the Universe, Arizona State University, Tempe, Arizona 85287, United States*

Joseph T. Perryman − *Department of Chemistry, University of California Davis, Davis, California 95616, United States*

Nicholas R. Singstock − *Department of Chemical and Biological Engineering, University of Colorado Boulder, Boulder, Colorado 80309, United States;* orcid.org/0000-0003-2093-0216

Mykola Abramchuk − *Peter A. Rock Thermochemistry Laboratory and NEAT ORU, University of California Davis, Davis, California 95616, United States;* orcid.org/0000-0003-4476-1322

Tamilarasan Subramani − *Peter A. Rock Thermochemistry Laboratory and NEAT ORU, University of California Davis, Davis, California 95616, United States*

Andy Lam − *Peter A. Rock Thermochemistry Laboratory and NEAT ORU, University of California Davis, Davis, California 95616, United States*

Ray Yoo − *Peter A. Rock Thermochemistry Laboratory and NEAT ORU, University of California Davis, Davis, California 95616, United States*

Jessica C. Ortiz-Rodríguez − *Department of Chemistry, University of California Davis, Davis, California 95616, United States*

Complete contact information is available at:

https://pubs.acs.org/10.1021/acs.chemmater.0c02648

Author Contributions

[⊥]K.L., J.T.P., and N.R.S. contributed equally to the manuscript. K.L., M.A., T.S., A.L., and R.Y. performed all drop solution calorimetry experiments. J.T.P. and J.C.O.-R. performed all synthesis, X-ray absorption spectroscopy, X-ray diffraction, and scanning electron microscopy experiments. N.R.S. performed all computational modeling. The manuscript was written through contributions of all authors. All authors have given approval to the final version of the manuscript.

Funding

Calorimetric studies were supported by the U.S. Department of Energy Office of Basic Energy Science, Grant DE-FG02-03ER46053.

Notes

The authors declare no competing financial interest.

■ ACKNOWLEDGMENTS

We would like to acknowledge the University of California Davis for start-up funding for this work, as well as support from the Cottrell Scholar program supported by the Research Corporation for Science Advancement (RCSA Grant ID 26780). J.T.P. would like to acknowledge support from the Ernest E. Hill Memorial Graduate Student Fellowship. C.B.M. and N.R.S. were supported by the U.S. National Science Foundation (Awards CBET-1806079 and CHE-1800592). N.R.S. was also supported by a U.S. Department of Education Graduate Assistance in Areas of National Need Fellowship under the Materials for Energy Conversion and Sustainability program. J.C.O.-R. was supported by the NSF Graduate Research Fellowship, grant no. 1650042. Use of the Stanford Synchrotron Radiation Lightsource, SLAC National Accelerator Laboratory, is supported by the U.S. Department of Energy, Office of Science, Office of Basic Energy Sciences under Contract No. DE-AC02-76SF00515. The SSRL Structural Molecular Biology Program is supported by the DOE Office of Biological and Environmental Research and by the National Institutes of Health, National Institute of General Medical Sciences (P41GM103393). Expenses related to calorimeter operation were supported by DE-FG02-03ER46053: "Thermodynamic Controls on the Synthesis, Structure and Reactivity of Materials for Energy" Department of Energy, Office of Science (DOE), Office of Basic Energy Sciences (BES), Materials Science and Engineering Division (MSED). The contents of this publication are solely the responsibility of the authors and do not necessarily represent the official views of NIGMS or NIH.

■ REFERENCES

(1) Levi, M. D.; Lancry, E.; Gizbar, H.; Lu, Z.; Levi, E.; Gofer, Y.; Aurbach, D. Kinetic and Thermodynamic Studies of Mg^{2+} and Li^{+} Ion Insertion into the Mo_6S_8 Chevrel Phase. *J. Electrochem. Soc.* **2004**, *151* (7), A1044.

(2) Ling, C.; Suto, K. Thermodynamic Origin of Irreversible Magnesium Trapping in Chevrel Phase Mo_6S_8: Importance of Magnesium and Vacancy Ordering. *Chem. Mater.* **2017**, *29* (8), 3731−3739.

(3) Levi, M. D.; Lancri, E.; Levi, E.; Gizbar, H.; Gofer, Y.; Aurbach, D. The effect of the anionic framework of Mo_6X_8 Chevrel Phase (X = S, Se) on the thermodynamics and the kinetics of the electrochemical insertion of Mg^{2+} ions. *Solid State Ionics* **2005**, *176* (19), 1695−1699.

(4) Chevrel, R.; Hirrien, M.; Sergent, M. Superconducting Chevrel phases: prospects and perspectives. *Polyhedron* **1986**, *5* (1), 87−94.

(5) Chevrel, R.; Sergent, M. *Superconductivity in Ternary Compounds I*; Springer-Verlag: Berlin, 1982; Vol. *32*, p 286.

(6) Fischer, Ø. Chevrel phases: Superconducting and normal state properties. *Appl. Phys.* **1978**, *16* (1), 1−28.

(7) Perryman, J. T.; Ortiz-Rodríguez, J. C.; Jude, J. W.; Hyler, F. P.; Davis, R. C.; Mehta, A.; Kulkarni, A. R.; Patridge, C. J.; Velázquez, J. M. Metal-promoted Mo_6S_8 clusters: a platform for probing ensemble effects on the electrochemical conversion of CO_2 and CO to methanol. *Mater. Horiz.* **2020**, *7* (1), 193−202.

(8) Jiang, J.; Gao, M.; Sheng, W.; Yan, Y. Hollow Chevrel-Phase $NiMo_3S_4$ for Hydrogen Evolution in Alkaline Electrolytes. *Angew. Chem., Int. Ed.* **2016**, *55* (49), 15240−15245.

(9) Peña, O. Chevrel phases: Past, present and future. *Phys. C* **2015**, *514*, 95−112.

(10) Geng, L.; Scheifers, J. P.; Zhang, J.; Bozhilov, K. N.; Fokwa, B. P. T.; Guo, J. Crystal Structure Transformation in Chevrel Phase Mo_6S_8 Induced by Aluminum Intercalation. *Chem. Mater.* **2018**, *30* (23), 8420−8425.

(11) Cheng, Y.; Parent, L. R.; Shao, Y.; Wang, C.; Sprenkle, V. L.; Li, G.; Liu, J. Facile Synthesis of Chevrel Phase Nanocubes and Their Applications for Multivalent Energy Storage. *Chem. Mater.* **2014**, *26* (17), 4904−4907.

(12) Attias, R. S.; Chae, M.; Dlugatch, B.; Oliel, M.; Goffer, Y.; Aurbach, D. The Role of Surface Adsorbed Cl^{-} complexes in Rechargeable Magnesium Batteries. *ACS Catal.* **2020**, *10*, 7773−7784.

(13) Alonso-Vante, N. Chevrel phases and chalcogenides. In *Handbook of Fuel Cells*; John Wiley and Sons Ltd.: 2010; pp 1−10.

(14) Chevrel, R.; Sergent, M.; Prigent, J. Un nouveau sulfure de molybdene: Mo_3S_4 preparation, proprietes et structure cristalline. *Mater. Res. Bull.* **1974**, *9* (11), 1487−1498.

(15) Murgia, F.; Antitomaso, P.; Stievano, L.; Monconduit, L.; Berthelot, R. Express and low-cost microwave synthesis of the ternary Chevrel phase $Cu_2Mo_6S_8$ for application in rechargeable magnesium batteries. *J. Solid State Chem.* **2016**, *242*, 151−154.

(16) Gershinsky, G.; Haik, O.; Salitra, G.; Grinblat, J.; Levi, E.; Daniel Nessim, G.; Zinigrad, E.; Aurbach, D. Ultra fast elemental synthesis of high yield copper Chevrel phase with high electrochemical performance. *J. Solid State Chem.* **2012**, *188*, 50−58.

(17) Sun, Y.; Xu, W.; Hou, W.; Wang, Y.; Wang, T.; Wu, L.; Xu, X.; Zhang, Y.; Zhou, X.; Du, Y.; Zhong, W. A facile reduction treatment to derive Mo_6S_8 from exfoliated MoS_2 for efficient microwave absorption applications. *Mater. Res. Express* **2019**, *6* (8), 085049.

(18) Agiorgousis, M. L.; Sun, Y.-Y.; West, D.; Zhang, S. Intercalated Chevrel Phase Mo_6S_8 as a Janus Material for Energy Generation and Storage. *ACS Applied Energy Materials* **2018**, *1* (2), 440−446.

(19) Wan, L. F.; Perdue, B. R.; Apblett, C. A.; Prendergast, D. Mg Desolvation and Intercalation Mechanism at the Mo_6S_8 Chevrel Phase Surface. *Chem. Mater.* **2015**, *27* (17), 5932−5940.

(20) Aurbach, D.; Lu, Z.; Schechter, A.; Gofer, Y.; Gizbar, H.; Turgeman, R.; Cohen, Y.; Moshkovich, M.; Levi, E. Prototype systems for rechargeable magnesium batteries. *Nature* **2000**, *407*, 724.

(21) Mao, M.; Lin, Z.; Tong, Y.; Yue, J.; Zhao, C.; Lu, J.; Zhang, Q.; Gu, L.; Suo, L.; Hu, Y.-S.; Li, H.; Huang, X.; Chen, L. Iodine Vapor Transport-Triggered Preferential Growth of Chevrel Mo_6S_8 Nanosheets for Advanced Multivalent Batteries. *ACS Nano* **2020**, *14* (1), 1102−1110.

(22) Liu, F.; Wang, T.; Liu, X.; Fan, L.-Z. Challenges and Recent Progress on Key Materials for Rechargeable Magnesium Batteries. *Adv. Energy Mater.* **2020**, 2000787.

(23) Choi, S.-H.; Kim, J.-S.; Woo, S.-G.; Cho, W.; Choi, S. Y.; Choi, J.; Lee, K.-T.; Park, M.-S.; Kim, Y.-J. Role of Cu in Mo_6S_8 and Cu Mixture Cathodes for Magnesium Ion Batteries. *ACS Appl. Mater. Interfaces* **2015**, *7* (12), 7016−7024.

(24) Caillat, T.; Fleurial, J. P.; Snyder, G. J. Potential of Chevrel phases for thermoelectric applications. *Solid State Sci.* **1999**, *1* (7), 535−544.

(25) Kurosaki, K.; Kosuga, A.; Yamanaka, S. Thermoelectric properties of Chevrel phase $Mo_6Te_{8-x}S_x$. *J. Alloys Compd.* **2003**, *351* (1), 208−211.
(26) Liu, P.; Choi, Y.; Yang, Y.; White, M. G. Methanol synthesis from H_2 and CO_2 on a Mo_6S_8 cluster: a density functional study. *J. Phys. Chem. A* **2010**, *114* (11), 3888−3895.
(27) Liu, C.; Liu, P. Mechanistic Study of Methanol Synthesis from CO_2 and H_2 on a Modified Model Mo_6S_8 Cluster. *ACS Catal.* **2015**, *5* (2), 1004−1012.
(28) Ortiz-Rodríguez, J. C.; Singstock, N. R.; Perryman, J. T.; Hyler, F. P.; Jones, S. J.; Holder, A. M.; Musgrave, C. B.; Velazquez, J. M. Stabilizing hydrogen adsorption through theory-guided chalcogen substitution in Chevrel-phase Mo_6X_8 (X = S, Se, Te) electrocatalysts. *ACS Appl. Mater. Interfaces* **2020**, DOI: 10.1021/acsami.0c07207.
(29) Wan, L. F.; Wright, J.; Perdue, B. R.; Fister, T. T.; Kim, S.; Apblett, C. A.; Prendergast, D. Revealing electronic structure changes in Chevrel phase cathodes upon Mg insertion using X-ray absorption spectroscopy. *Phys. Chem. Chem. Phys.* **2016**, *18* (26), 17326−17329.
(30) Thole, F.; Wan, L. F.; Prendergast, D. Re-examining the Chevrel phase Mo_6S_8 cathode for Mg intercalation from an electronic structure perspective. *Phys. Chem. Chem. Phys.* **2015**, *17* (35), 22548−22551.
(31) Perryman, J. T.; Hyler, F. P.; Ortiz-Rodríguez, J. C.; Mehta, A.; Kulkarni, A. R.; Velázquez, J. M. X-ray absorption spectroscopy study of the electronic structure and local coordination of 1st row transition metal-promoted Chevrel-phase sulfides. *J. Coord. Chem.* **2019**, *72* (8), 1322−1335.
(32) Hammer, B.; Nørskov, J. K. Electronic factors determining the reactivity of metal surfaces. *Surf. Sci.* **1995**, *343* (3), 211−220.
(33) Nilsson, A.; Pettersson, L.; Hammer, B.; Bligaard, T. H.; Christensen, C. K.; Nørskov, J. The electronic structure effect in heterogeneous catalysis. *Catal. Lett.* **2005**, *100*, 111−114.
(34) Bligaard, T.; Nørskov, J. K. Ligand effects in heterogeneous catalysis and electrochemistry. *Electrochim. Acta* **2007**, *52* (18), 5512−5516.
(35) Yvon, K.; Paoli, A. Charge transfer and valence electron concentration in Chevrel phases. *Solid State Commun.* **1977**, *24* (1), 41−45.
(36) Peña, O.; Sergent, M. Rare earth based chevrel phases $REMo_6X_8$: Crystal growth, physical and superconducting properties. *Prog. Solid State Chem.* **1989**, *19* (3), 165−281.
(37) Hughbanks, T.; Hoffmann, R. Molybdenum chalcogenides: clusters, chains, and extended solids. The approach to bonding in three dimensions. *J. Am. Chem. Soc.* **1983**, *105* (5), 1150−1162.
(38) Lancry, E.; Levi, E.; Gofer, Y.; Levi, M.; Salitra, G.; Aurbach, D. Leaching Chemistry and the Performance of the Mo_6S_8 Cathodes in Rechargeable Mg Batteries. *Chem. Mater.* **2004**, *16* (14), 2832−2838.
(39) Levi, E.; Gofer, Y.; Vestfreed, Y.; Lancry, E.; Aurbach, D. $Cu_2Mo_6S_8$ Chevrel Phase, A Promising Cathode Material for New Rechargeable Mg Batteries: A Mechanically Induced Chemical Reaction. *Chem. Mater.* **2002**, *14* (6), 2767−2773.
(40) Levi, E.; Aurbach, D. Chevrel Phases, $M_xMo_6T_8$ (M = Metals, T = S, Se, Te) as a Structural Chameleon: Changes in the Rhombohedral Framework and Triclinic Distortion. *Chem. Mater.* **2010**, *22* (12), 3678−3692.
(41) Hinode, H.; Ohira, Y.; Wakihara, M. Measurements of the formation enthalpy of Mo_6S_{8-y} clusters. *Thermochim. Acta* **1996**, *282−283*, 331−343.
(42) Uchida, T.; Wakihara, M. Thermal behavior of the chevrel phase sulfides. *Thermochim. Acta* **1991**, *174*, 201−221.
(43) Levin, E. E.; Grebenkemper, J. H.; Pollock, T. M.; Seshadri, R. Protocols for High Temperature Assisted-Microwave Preparation of Inorganic Compounds. *Chem. Mater.* **2019**, *31* (18), 7151−7159.
(44) Chandrasekaran, S.; Basak, T.; Srinivasan, R. Microwave heating characteristics of graphite based powder mixtures. *Int. Commun. Heat Mass Transfer* **2013**, *48*, 22−27.
(45) Yun, Y.; Park, J.; Kim, H.; Bae, J. J.; Joo, M.-K.; Suh, D. Electrothermal Local Annealing via Graphite Joule Heating on Two-Dimensional Layered Transistors. *ACS Appl. Mater. Interfaces* **2018**, *10* (30), 25638−25643.
(46) Navrotsky, A. Progress and new directions in high temperature calorimetry revisited. *Phys. Chem. Miner.* **1997**, *24* (3), 222−241.
(47) Navrotsky, A. Progress and new directions in high temperature calorimetry. *Phys. Chem. Miner.* **1977**, *2* (1), 89−104.
(48) Navrotsky, A. Progress and New Directions in Calorimetry: A 2014 Perspective. *J. Am. Ceram. Soc.* **2014**, *97* (11), 3349−3359.
(49) Hayun, S.; Salhov, S.; Lilova, K.; Navrotsky, A. Enthalpies of Formation of High Entropy and Multicomponent Alloys using Oxide Melt Solution Calorimetry. *Intermetallics* **2020**, *125*, 106897.
(50) Abramchuk, M.; Lilova, K.; Subramani, T.; Yoo, R.; Navrostky, A. Development of high-temperature oxide melt solution calorimetry for p-block element containing materials. *J. Mater. Res.* **2020**, 1.
(51) Kresse, G.; Furthmüller, J. Efficient iterative schemes for ab initio total-energy calculations using a plane-wave basis set. *Phys. Rev. B: Condens. Matter Mater. Phys.* **1996**, *54* (16), 11169−11186.
(52) Sun, J.; Ruzsinszky, A.; Perdew, J. P. Strongly Constrained and Appropriately Normed Semilocal Density Functional. *Phys. Rev. Lett.* **2015**, *115* (3), 036402.
(53) Manz, T. A.; Limas, N. G. Introducing DDEC6 atomic population analysis: part 1. Charge partitioning theory and methodology. *RSC Adv.* **2016**, *6* (53), 47771−47801.
(54) Ong, S. P.; Richards, W. D.; Jain, A.; Hautier, G.; Kocher, M.; Cholia, S.; Gunter, D.; Chevrier, V. L.; Persson, K. A.; Ceder, G. Python Materials Genomics (pymatgen): A robust, open-source python library for materials analysis. *Comput. Mater. Sci.* **2013**, *68*, 314−319.
(55) Maintz, S.; Deringer, V. L.; Tchougréeff, A. L.; Dronskowski, R. LOBSTER: A tool to extract chemical bonding from plane-wave based DFT. *J. Comput. Chem.* **2016**, *37* (11), 1030−1035.
(56) Sun, W.; Bartel, C. J.; Arca, E.; Bauers, S. R.; Matthews, B.; Orvañanos, B.; Chen, B.-R.; Toney, M. F.; Schelhas, L. T.; Tumas, W.; Tate, J.; Zakutayev, A.; Lany, S.; Holder, A. M.; Ceder, G. A map of the inorganic ternary metal nitrides. *Nat. Mater.* **2019**, *18*, 732−739.
(57) *Inorganic Crystal Structure Database*; FIZ Karlsruhe, 2020. https://icsd.fiz-karlsruhe.de.
(58) Kunzl, V. A linear dependence of energy levels on the valency of elements. *Collect. Czech. Chem. Commun.* **1932**, *4*, 213−224.
(59) Glasser, L. Solid-State Energetics and Electrostatics: Madelung Constants and Madelung Energies. *Inorg. Chem.* **2012**, *51* (4), 2420−2424.
(60) Herman, M. A.; Richter, W.; Sitter, H. *Epitaxy - Physical Principles and Technical Implementation*; Springer-Verlag: Berlin, 2004; p 525.
(61) Shannon, R. Revised effective ionic radii and systematic studies of interatomic distances in halides and chalcogenides. *Acta Crystallogr., Sect. A: Cryst. Phys., Diffr., Theor. Gen. Crystallogr.* **1976**, *32* (5), 751−767.
(62) Chase, M. W. *NIST-JANAF Thermochemical Tables*, 4th ed.; Journal of Physical and Chemical Reference Data Monographs 9; American Institute of Physics: 1998.
(63) Seghir, S.; Stein, N.; Boulanger, C.; Lecuire, J. M. Electrochemical determination of the diffusion coefficient of cations into Chevrel phase-based electrochemical transfer junction by potential step chronoamperometry and impedance spectroscopy. *Electrochim. Acta* **2011**, *56* (6), 2740−2747.
(64) Mei, L.; Xu, J.; Wei, Z.; Liu, H.; Li, Y.; Ma, J.; Dou, S. Chevrel Phase Mo_6T_8 (T = S, Se) as Electrodes for Advanced Energy Storage. *Small* **2017**, *13* (34), 1701441.